Sol-gel-processed amorphous-phase ZrO_2 based resistive random access memory

Materials Research Express

PAPER

Sol-gel-processed amorphous-phase ZrO_2 based resistive random access memory

Kyoungdu Kim[1], **Woongki Hong**[2], **Changmin Lee**[1], **Won-Yong Lee**[1], **Do Won Kim**[1], **Hyeon Joong Kim**[1], **Hyuk-Jun Kwon**[2,3], **Hongki Kang**[2,*] **and Jaewon Jang**[1,4,*]

[1] School of Electronic and Electrical Engineering, Kyungpook National University, Daegu 41566, Republic of Korea
[2] Department of Information and Communication Engineering, DGIST, Daegu 42988, Republic of Korea
[3] Convergence Research Advanced Centre for Olfaction, DGIST, Daegu 42988, Republic of Korea
[4] School of Electronic Engineering, Kyungpook National University, Daegu 41566, Republic of Korea
[*] Authors to whom any correspondence should be addressed.

E-mail: hkang@dgist.ac.kr **and** j1jang@knu.ac.kr

Keywords: sol-gel, ZrO_2, resistive random access memory, amorphous phase, electrochemical metallization cell

OPEN ACCESS

RECEIVED
4 September 2021

REVISED
25 October 2021

ACCEPTED FOR PUBLICATION
27 October 2021

PUBLISHED
10 November 2021

Abstract

In this study, sol–gel-processed amorphous-phase ZrO_2 was used as an active channel material to improve the resistive switching properties of resistive random access memories (RRAMs). ITO/ZrO_2/Ag RRAM devices exhibit the properties of bipolar RRAMs. The effect of the post-annealing temperature on the electrical properties of the ZrO_2 RRAM was investigated. Unlike the ZrO_2 films annealed at 400 and 500 °C, those annealed at 300 °C were in amorphous phase. The RRAM based on the amorphous-phase ZrO_2 exhibited an improved high-resistance state (HRS) to low-resistance state ratio (over 10^6) as well as promising retention and endurance characteristics without deterioration. Furthermore, its disordered nature, which causes efficient carrier scattering, resulted in low carrier mobility and the lowest leakage current, influencing the HRS values.

1. Introduction

Modeled after the human brain, neuromorphic computing systems have great potential applications in next-generation electronic devices. Neuromorphic computing has emerged as an optimized approach for realizing real time interaction systems with various environments associated with autonomous applications such as robotics or face classification [1, 2]. However, to realize a neuromorphic computing system using conventional memories and circuits, the scaling issue needs to be resolved. In general, conventional memories and circuits require physical separation between them [3]. Moreover, the neuromorphic computing system requires greater device density to realize human-like operations; therefore, a new device concept, demonstrating extreme scalability, is needed to overcome Moore's law. A variety of conventional flash memory devices and resistive random access memory (RRAM) devices have been considered promising candidates with extreme scalability (<10 nm) and improved power consumption efficiency [4–6]. A transistor–one RRAM structure is utilized to solve the sneak path issue while fabricating the RRAM array [7, 8]. According to numerous studies, ZrO_2 is considered a promising active channel layer for RRAM [9–11]. Moreover, the performance of thin-film transistors (TFTs) is remarkably improved using a ZrO_2 insulator for TFTs [12–14]. Thus, ZrO_2 can be simultaneously used as an insulator for transistors and an active channel layer, resulting in reduced manufacturing steps.

The sol-gel process is an easy and simple method to obtain high-quality metal oxide layers. The solution phase precursor allows sufficient amounts of ink for spin-coating, dip coating, and printing processes for large-area applications without using the conventional vacuum-based high-cost deposition tools.

In this study, a sol–gel-processed ZrO_2 layer was used as the active channel layer in RRAM. The structural, chemical and electrical characteristics of the ZrO_2 active channel layers for RRAM were investigated as a function of the post-annealing temperatures (300 °C, 400 °C, and 500 °C). ZrO_2 films annealed at 300 °C

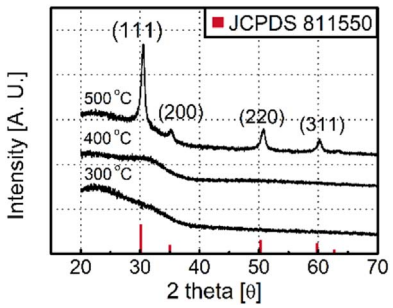

Figure 1. GIXRD patterns of sol–gel-processed ZrO_2 layers at different annealing temperatures.

showed an amorphous phase. The RRAM comprising ZrO_2 films annealed at 300 °C showed an improved high resistance state (HRS) to low-resistance state (LRS) ratio ($>10^6$) with promising retention and endurance characteristics. The endurance and retention lasted 10^2 cycles and 10^3 s, respectively, without deterioration. In addition, the 300 °C annealing process has the potential to fabricate flexible ZrO_2 RRAM devices on polyimide substrates with high glass transition temperature (311 °C).

2. Methods

2.1. Fabrication process

In this study, 0.001 mol of zirconium (IV) acetylacetonate ($Zr(C_5H_7O_2)_4$) from Sigma Aldrich was used as a precursor. It was dissolved in 9.9 ml of ethanol, and 0.1 ml of ethanolamine (Sigma Aldrich) was added as a capping material. The ultrasonication process was performed for 1 h at room temperature to clear the ZrO_2 precursor solution. Commercial indium tin oxide (ITO)-deposited glass substrates (Sigma Aldrich) were prepared to fabricate the ZrO_2 RRAM device. Before depositing ZrO_2, the substrates were cleaned using ultrasonic equipment for 10 min with acetone and deionized water. UV/O_3 treatment was performed for 10 min to eliminate contaminated organic debris and make the surfaces of ITO glass hydrophilic to ensure that the solution precursor was coated appropriately during the spin-coating process. The prepared precursor solution was deposited on ITO glass substrates using a spin-coating method (3000 rpm for 50 s). A soft-drying process at 150 °C for 10 min in air was employed to evaporate the solvent, and additional annealing processes were performed on the hot plates at 300 °C, 400 °C, and 500 °C for 3 h in air. Finally, 20 nm-thick ZrO_2 films were formed. A shadow mask was used in the thermal evaporator to form a 30 μm $\times$ 30 μm Ag layer, which served as the top electrode, and a 100 nm-thick Ag layer was deposited at a rate of 1 Å s^{-1} while maintaining a pressure of 5^{-6} Torr.

2.2. Analysis method

The structural features and phase were investigated by measuring the grazing incidence x-ray diffraction (GIXRD) via X'pert Pro with a Cu Kα wavelength of 1.54 Å and a small incident angle of 0.3°. X-ray photoelectron spectroscopy (XPS, Quantera SXM) was used to identify the elemental and chemical compositions. Film thickness was measured using a scanning probe microscope (Park NX20, tapping mode). An Agilent 4155 semiconductor parameter analyzer was run at room temperature to estimate the electrical characteristics of the air.

3. Results and discussions

Figure 1 shows the GIXRD spectra of sol–gel-processed ZrO_2 films annealed at 300 °C, 400 °C, and 500 °C. The ZrO_2 films annealed at 300 °C did not show any peaks, indicating amorphous-phase ZrO_2 films. Films annealed at 400 °C showed only one broad peak at 30.51°, whereas those annealed at 500 °C were consistent with cubic polycrystalline structured ZrO_2 films (JCPDS: 81–1550). In detail, a total of four diffraction peaks appeared at 30.51°, 35.17°, 50.77°, and 60.25°, representing the (111), (200), (220), and (311) orientations, respectively. Among them, ZrO_2 films primarily grew in the (111) direction. With an increase in annealing temperature, the intensity of the peaks also increased, indicating the enhanced crystallinity and grain growth of the deposited ZrO_2 films. Additionally, the preferential orientation peak, particularly for the (111) plane, became sharper and dominant as the post-annealing temperature increased. The Scherrer equation was used to determine the crystalline size; this equation was applied to the full width at half maximum of a peak observed in the GIXRD

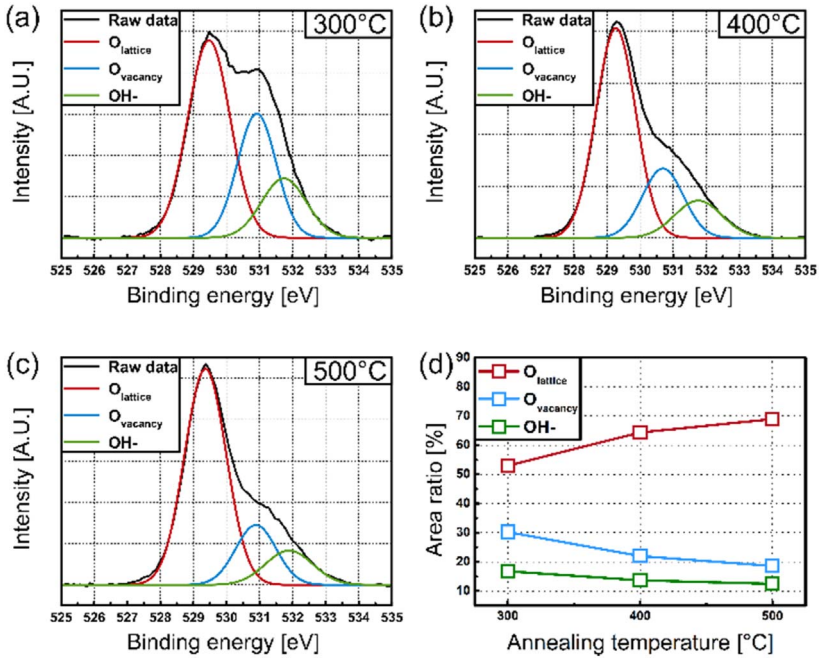

Figure 2. (a) Oxygen 1s XPS of sol–gel-processed ZrO_2 thin films with different annealing temperatures: (a) 300 °C, (b) 400 °C, and (c) 500 °C. (d) The respective occupancy ratio of $O_{Lattice}$, $O_{Vacancy}$ and –OH groups in ZrO_2 films.

spectra.

$$D = \frac{0.9\lambda}{\beta \cos\theta} \tag{1}$$

where λ is the x-ray wavelength, β is the width at half the peak value, and θ is the Bragg angle. The calculated crystalline size of the ZrO_2 film annealed at 400 °C and 500 °C were 2.3 and 13.3 nm, respectively.

Figures 2(a)–(c) shows the O1s XPS spectra of ZrO_2 films obtained as a function of the annealing temperature. The O1s spectra have three peaks positioned at 530.0, 531.4, and 532.2 eV, representing three states of oxygen ions. The oxygen ions (O^{2-}), called $O_{Lattice}$, which combined with metal cations and turned into ZrO_2, are shown at the 530.0 eV peak. The oxygen vacancies at medium binding energy, called $O_{Vacancy}$, are signified at the 531.4 eV peak. The peak corresponding to the OH group and/or aqueous molecules adsorbed on the surface of the ZrO_2 films is positioned at the 532.2 eV peak. Figure 3(d) shows the area ratio of $O_{Lattice}$, $O_{Vacancy}$, and –OH groups as a function of the post-annealing temperature. As the post-annealing temperature increased, $O_{Lattice}$ started to increase; however, the $O_{Vacancy}$ and –OH groups started decreasing simultaneously. More oxygen vacancies can be filled by free oxygen atoms from the outside at high temperatures. The dynamic energy of oxygen atoms increased, and they entered ZrO_2 and easily filled the oxygen vacancies at elevated temperatures. Finally, they were converted into oxygen ions, combined with metal cations ($O_{Lattice}$), after cooling.

The I–V curves at different annealing temperatures are shown in figures 3(a) and (b). All ZrO_2-based RRAM devices exhibited conventional bipolar characteristics. Initially, the fabricated ITO/ZrO_2/Ag devices were in a HRS. When voltage was applied from negative (−10.0 V) to positive (+7.0 V), the current increased abruptly at approximately +2.0 V, and the devices entered a LRS. The voltage at which the current suddenly increases is called the SET voltage. In contrast, when a negative voltage bias was applied from +7.0 V to −10.0 V, the current decreased suddenly, turning into HRS. Binary metal oxides, such as Nb_2O_3, TiO_2, and ZrO_2, exhibit resistive switching memory behavior, originating from the formation and destruction of a conductive path with two representative mechanisms: (1) oxygen vacancy-based conductive path within the active metal oxide layers and (2) metallic conductive path formation, originating from oxidation and reduction processes from electrochemical metal electrodes such as Ag or Cu. In this study, the primary mechanism is the metallic conductive path formation, which originates from the oxidation and reduction processes from the top Ag electrode. When voltage was applied from negative (−10.0 V) to positive (+7.0 V), Ag at the interface between the top Ag electrode and ZrO_2 films started to oxidize and diffused into the ZrO_2 films, resulting in conductive Ag filament formation. The formed Ag filament contacts the bottom ITO electrodes, changing the resistance states from HRS to LRS. Alternatively, when a negative voltage bias was applied from +7.0 V to −10.0 V, the

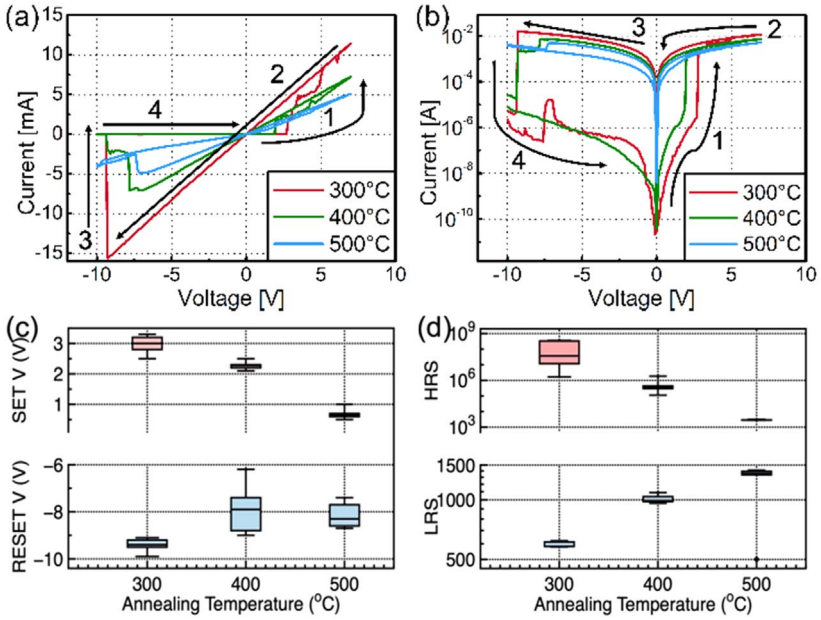

Figure 3. I–V curves for (a) the Ag/ZrO_2/ITO RRAM devices depending at different annealing temperatures on a linear scale and (b) the Ag /ZrO_2/ITO RRAM devices on the log scale. (c) SET/RESET ratio values. (d) HRS/LRS ratio values. (measured device size: 30 μm $\times$ 30 μm, read voltage: +0.1 V.

previously formed conductive Ag filaments were broken by the reduction process and the resistance state returned from LRS to HRS.

Figure 3(c) shows the SET and RESET voltages as a function of post-annealing temperature. The SET and RESET voltages for the amorphous-phase ZrO_2 samples annealed at 300 °C are higher than those of the polycrystalline phase ZrO_2 samples annealed at 500 °C. Based on the GIXRD data, the ZrO_2 films annealed at 300 °C were amorphous, whereas those annealed at 500 °C were polycrystalline. Normally, the grain boundary accelerates ion migration that decreases the SET voltage [15]. In addition, larger grains and fewer grain boundaries reduced the Ag filament formation, making the Ag filament easy to break and lowering the RESET voltages. Therefore, the SET/RESET values of the RRAM comprising amorphous-phase ZrO_2 annealed at 300 °C were the highest.

Figure 3(d) shows the HRS and LRS values of fabricated ZrO_2 RRAM devices. The HRS/LRS ratios at 400 °C and 500 °C were approximately 10^3 and 10^1, respectively. However, at 300 °C, a substantial HRS/LRS ratio of $>10^6$ is observed. It is well known that oxygen vacancy (O_V) can intensify the leakage current [16]. O_Vs are generally regarded as defects in the oxide that act as traps and enable trap-assisted tunneling or hopping mechanisms, thereby boosting the leakage current phenomenon. However, the RRAM based on ZrO_2 annealed at 500 °C showed the lowest HRS values and the largest leakage current, while the O_V concentration was the lowest based on XPS analysis. ZrO_2 film phase plays a critical role in the leakage current mechanism. Compared with the ZrO_2 films annealed at 400 °C and 500 °C, the ZrO_2 films annealed at 300 °C showed an amorphous phase. The carrier's disordered nature and efficient scattering lead to low carrier mobility and the lowest leakage current, influencing the HRS values [17–19].

The J–V relationship was investigated to explain the current conduction mechanism of Ag/ZrO_2/ITO devices as a function of the post-annealing temperature. The positive and negative regions of the double logarithmic plot of the J–V curves are shown in figure 4. Furthermore, the relationship between the current and bias voltage of the LRS and initial HRS was linear, followed by the Ohmic conduction based on the following equation:

$$J = \frac{qn_0\mu V}{d} \tag{2}$$

where q is the elementary charge, n0 is the carrier concentration, μ is the carrier mobility, and d is the thickness of the ZrO_2 layer. In an HRS, the slope of the double logarithmic plot changed from 1 to 2 as V increased. In other metal oxide RRAM devices, the initial transport mechanism was Ohmic, followed by the Child's square law region, where the current is proportional to V^2. Additionally, the Poole–Frenkel (P–F) emission mechanism is dominant during the transition from HRS to LRS. For reference, equation (2) is a P–F emission formula, and the linear section follows P–F emission by fitting ln(J/E) versus $E^{0.5}$.

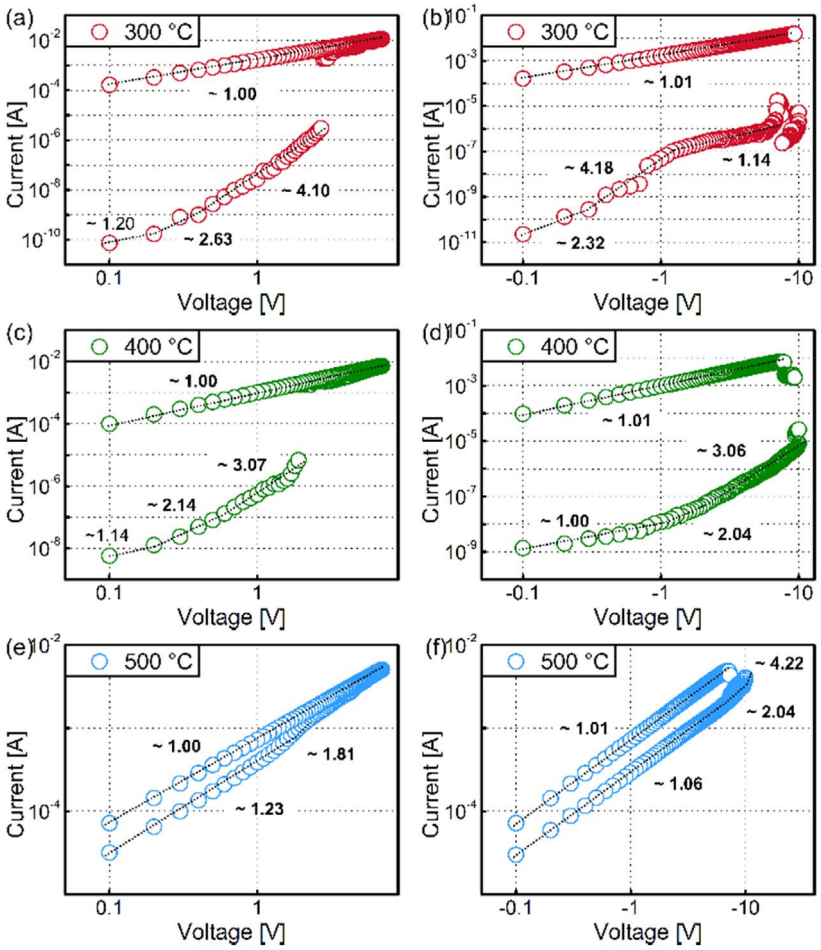

Figure 4. (a) Positive and negative regions of double logarithmic plot of J–V curves as a function of the post-annealing temperature: (a), (c), (e) positive and (b), (d), (f) negative voltage regions.

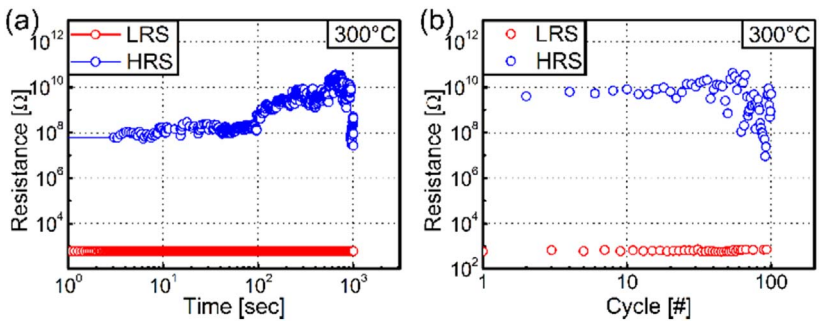

Figure 5. (a) Retention characteristics of sol–gel-processed Ag/ZrO_2/ITO RRAM and (b) endurance characteristics of the Ag/ZrO_2/ITO RRAM.

$$J = (q\mu N_C E)\exp\left\{-q\left[\phi_T - \left(\frac{qE}{\pi\varepsilon_0\varepsilon_d}\right)^{0.5}\right]/k_B T\right\} \quad (3)$$

where q is elementary charge, μ is the electron's mobility due to drift, N_C is the density of states inside the conduction band, E is the electrical field, ϕ_T is the potential energy due to traps or defects, kB is the Boltzmann constant, T is the temperature [K], and εd is the dielectric constant inherent to ZrO_2 [20]. The fitting of ln(J/E) versus $E^{0.5}$ reveals that the P–F transport mechanism is the primary transport mechanism under the HRS condition, regardless of post-annealing temperatures.

Retention and endurance are usually measured to verify the performance of the Ag/300 °C annealed ZrO_2/ITO RRAM device, which has the highest HRS/LRS ratio. The HRS and LRS values were obtained at a

read voltage of +0.1 V. The HRS/LRS ratio (over 10^6) of the RRAM based on ZrO_2 annealed at 300 °C were the highest and lasted for up to 10^3 programs/erase cycles. Moreover, the LRS and HRS lasted for approximately 10^3 s, with minimal degradation.

4. Conclusion

In this study, a ZrO_2 RRAM device was fabricated using the sol–gel method and devices with the best characteristics were studied by varying the annealing temperature. The ZrO_2 films annealed at 300 °C showed an amorphous-phase ZrO_2. RRAM based on amorphous-phase ZrO_2 shows an improved HRS/LRS ratio ($>10^6$) with promising retention and endurance characteristics. Its endurance and retention lasted for 10^2 cycles and 10^3 s, respectively, without deterioration. The disordered structures of the amorphous materials lead to low carrier mobility and the lowest leakage current, thereby influencing the HRS value.

Acknowledgments

This research was supported by the Basic Science Research Program through the National Research Foundation of Korea (NRF) grant funded by the Korea government (MSIT) (2019R1F1A1059788).

Data availability statement

No new data were created or analysed in this study.

ORCID iDs

Jaewon Jang https://orcid.org/0000-0003-1908-0015

References

[1] LeCun Y, Bengio Y and Hinton G 2015 Deep learning *Nature* **521** 436–44
[2] Furber S 2016 Large-scale neuromorphic computing systems *J. Neural Eng.* **13** 051001
[3] Shulaker M M, Hills G, Park R S, Howe R T, Saraswat K, Wong H S P and Mitra S 2017 Three-dimensional integration of nanotechnologies for computing and data storage on a single chip *Nature* **547** 74–8
[4] Zahoor F, Azni Zulkifli T Z and Khanday F A 2020 Resistive random access memory (rram): an overview of materials, switching mechanism, performance, multilevel cell (mlc) storage, modeling, and applications *Nanoscale Res. Lett.* **15** 90
[5] Chand U, Huang C Y, Kumar D and Tseng T Y 2015 Metal induced crystallized poly-Si-based conductive bridge resistive switching memory device with one transistor and one resistor architecture *Appl. Phys. Lett.* **107** 203502
[6] Waser R and Aono M 2007 Nanoionics-based resistive switching memories *Nat. Mater.* **6** 833–40
[7] Liu H, Lv H, Yang B, Xu X, Liu R, Liu Q, Long S and Liu M 2014 Uniformity improvement in 1T1R RRAM with gate voltage ramp programming *IEEE Electron Device Lett.* **35** 1224–6
[8] Wang Z R, Su Y T, Li Y, Zhou Y Z, Chu J T, Chang K C, Chang T C, Tsai T M, Sze S M and Miao X S 2017 Functionally complete boolean logic in 1T1R resistive random access memory *IEEE Electron Deve Lett.* **30** 179–82
[9] Jang J and Subramanian V 2017 Effect of electrode material on resistive switching memory behavior of solution-processed resistive switches: realization of robust multi-level cells *Thin Solid Films* **625** 87–92
[10] Lee S, Kim T, Jang B, Lee W, Song K, Kim H, Do G, Hwang S, Chung S and Jang J 2018 Impact of device area and film thickness on performance of sol-gel processed ZrO_2 RRAM *IEEE Electron Device Lett.* **39** 668–71
[11] Ha S, Lee H, Lee W Y, Jang B, Kwon H J, Kim K and Jang J 2019 Effect of annealing environment on the performance of sol-gel processed ZrO_2 RRAM *Electronics* **8** 947–54
[12] Jang J, Kitsomboonloha R, Swisher S L, Park E S, Kang H and Subramanian V 2013 transparent high-performance thin film transistors from solution-processed SnO_2/ZrO_2 gel-like precursors *Adv. Mater.* **25** 1042–7
[13] Jang J, Kang H, Chakravarthula H C N and Subramanian V 2015 Fully inkjet-printed transparent oxide thin film transistors using a fugitive wettability switch *Adv. Electron. Mater.* **1** 1500086
[14] Kwon H, Jang J and Grigoropoulos C P 2016 laser direct writing process for making electrodes and high-k sol–gel zro_2 for boosting performances of MoS_2 transistors *ACS Appl Mater Int.* **8** 9314–8
[15] Clarke H, Brown T, Hu J, Ganguli R, Reed A, Voevodin A and Shamberger P J 2016 Microstructure dependent filament forming kinetics in HfO_2 programmable metallization cells *Nanotechnology* **27** 425709
[16] Zhu X, Zhuge F, Li M, Yin K, Liu Y, Zuo Z, Chen B and Li R W 2011 Microstructure dependence of leakage and resistive switching behaviours in Ce-doped $BiFeO_3$ thin films *J. Phys. D: Appl. Phys.* **44** 415104–10
[17] Ram Kumar K and Satyam M 1998 Carrier mobility in polycrystalline semiconductors *Appl. Phys. Lett.* **39** 898
[18] Steinhauser J, Faÿ S, Oliveira N, Vallat-Sauvain E and Ballif C 2007 Transition between grain boundary and intragrain scattering transport mechanisms in boron-doped zinc oxide thin films *Appl. Phys. Lett.* **90** 142107
[19] Cai W, Zhu Z, Wei J, Fang Z, Ning H, Zheng Z, Zhou S, Yao R, Peng J and Lu X 2017 A simple method for high-performance, solution-processed, amorphous ZrO_2 gate insulator TFT with a high concentration precursor *Materials* **10** 972–82
[20] Sze S M 1967 Current transport and maximum dielectric strength of silicon nitride films *J. Appl. Phys.* **38** 2951